ELSEVIER

International Journal of Mass Spectrometry 177 (1998) 51–62

International Journal of Mass Spectrometry

Electron capture and energy loss in ~100 keV collisions of atomic and molecular ions on C_{60}

M.O. Larsson[a], P. Hvelplund[a,*], M.C. Larsen[a], H. Shen[a,1], H. Cederquist[b], H.T. Schmidt[b]

[a]*Institute of Physics and Astronomy, University of Aarhus, DK-8000, Århus C, Denmark*
[b]*Atomic Physics, Stockholm University, Frescativ. 24, S-10405, Stockholm, Sweden*

Received 2 January 1998; accepted 11 March 1998

Abstract

We have determined absolute attenuation and electron capture cross sections in ~100 keV collisions between atomic ions of moderate charge states (He^+, He^{2+}, Ar^{2+}, Ar^{3+}, Ar^{4+}, Xe^{2+}, Xe^{3+}, Xe^{4+}) and C_{60} molecules in the gas phase. The measured cross-sections support previous findings of the charge dynamics *within* C_{60} from electron capture experiments with higher ionic charges. For a non-negligible fraction of the capture events we observed substantial ionic energy loss ($\leq$2 keV), which is ascribed to collisions where the ion passes through the C_{60} molecule. Furthermore, we found that a molecular ion (100 keV CO_2^{2+}) that captures an electron from C_{60} can lose similar amounts of energy without dissociating. It is concluded that the predominant contribution to the ionic energy loss comes from electron excitation and ionization. (Int J Mass Spectrom 177 (1998) 51–62) © 1998 Elsevier Science B.V.

Keywords: Electron capture; Fullerene; Cross section; Energy loss spectra

1. Introduction

In recent years the properties of C_{60} and related fullerene compounds have attracted increasing interest among physicists and chemists in the field of ionic collisions. Fragmentation of fullerenes in gas-phase collisions have been studied extensively [1–7]. It is generally believed that the long-term response to the collisional activation is sequential evaporation of C_2 units, whereas less is known about the details of the rapid dissociation and the energy conversion in the collision. Another line of research is concerned with electron transfer in nondissociative collisions involving fullerenes [8–14]. Compared with pure atomic collisions, the introduction of fullerenes raises questions about the role of the many loosely bound electrons and the internal fullerene charge dynamics as well as the stability against Columbic explosion of multiply charged clusters [15]. Studies of ion–cluster collisions are important for a general understanding of ionic impact on finite-size objects and a unified picture of ion–atom [16] and ion–surface [17] collisions. Ionic collisions on clusters and insulators [18,19] have in particular much in common because captured electrons originate from a limited spatial region in both cases.

* Corresponding author.

[1] Present address: Institute of Modern Physics, Fudan University, Shanghai 200433, P.R. China.

PII S1387-3806(98)14029-0

Here we address electron capture and energy loss in slow (collision velocity lower than the Bohr velocity) ion–C_{60} collisions. Despite theoretical works [10,13] and cross-section measurements for capture from C_{60} by slow, highly charged atomic ions [11,20] and fullerene ions [9], there are still controversies regarding the C_{60} charge dynamics in the collision. According to the interpretations of the experimental results in the study by Shen et al. [9] and later in the study by Selberg et al. [11], the positive charge created in C_{60} on transfer of an electron remains fixed in position at the cage surface closest to the ion *during* the actual transfer, whereas relaxation to the most favourable charge configuration takes place between transfer events. That is, electron capture is assumed to be sequential in the sense that electrons are transferred one by one at separate points along the collision trajectory. By contrast, the cross-sections in the study by Walch et al. [20] could be accounted for by a model where the charge on C_{60} is localized in its centre. In this work we have tried to shed some light on this discrepancy by going to lower atomic charges for which a more sensitive dependence on the charge localization is expected. The calculation of the C_{60} density in the target vapour is crucial for the cross-section determinations, and our choice of the vapour pressure curve given in the work by Abrefah et al. [21] for this purpose is discussed in detail. Relying on this curve, as was done also in other studies [9,11,20], we obtain absolute cross-sections that support the static surface-charge model presented in Shen et al. [9] and Selberg et al. [11].

The most striking feature of the present data is probably that many moderately scattered ions lose large amounts of translational energy in the capture reactions. The relative importance of this process increases with the number of captured electrons and is most pronounced for final ionic charges of +1 (neutral collision products cannot be detected in the present experiment). We find that some of the reacted ions lose hundreds of electronvolts in translational energy. This situation is opposite to the one observed with projectiles of higher charge where energy-gain processes dominate [11,13]. The present energy-loss events are ascribed to cage-penetrating collisions. The contributions from inelastic electronic processes and elastic binary encounters between the ion and individual C atoms in C_{60} are discussed and compared with beam–foil results and theoretical estimates [22]. We conclude that the dominant energy-loss mechanism in the present collisions is electronic excitation and ionization. The ionic energy loss is an important measure in fragmentation studies because it, together with the initial thermal energy of C_{60}, gives the maximum available energy for the dissociation and ionization processes.

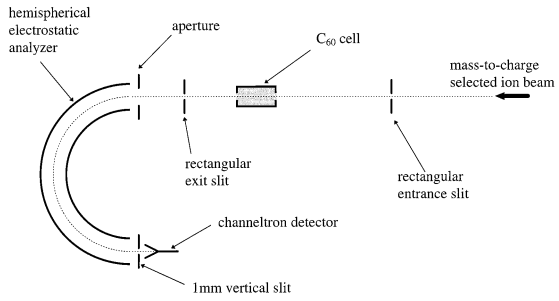

Fig. 1. Schematic drawing of the experimental set-up. The C_{60} target cell is 30 mm long with entrance and exit aperture diameters of 1 and 2 mm, respectively. The distance between the C_{60} cell and the electrostatic analyzer aperture is 700 mm, which together with the aperture diameter 10 mm gives an acceptance angle of 0.4° for the analyzer. The electrode separation and radius of the analyzer are 15 and 150 mm, respectively.

2. Experimental

A more detailed description of the setup, of which the essential parts are displayed in Fig. 1, is given in Shen et al. [9]. Atomic and molecular ions from a plasma–discharge ion source were accelerated to translational energies of 100 or 133 keV and charge-to-mass selected by a double-focusing dipole magnet of radius 2 m. The selected ion beam (He^+, He^{2+}, Ar^{2+}, Ar^{3+}, Ar^{4+}, Xe^{2+}, Xe^{3+}, Xe^{4+}, or CO_2^{2+}) was directed through the C_{60} gas target—a heated stainless steel cylinder partly filled with 99.9% pure C_{60} powder (Hoechst gold grade, not redistilled). Before starting the measurements the target was preheated to 480 °C for reasons to be discussed. The target pressure was determined from the C_{60} vapor pressure

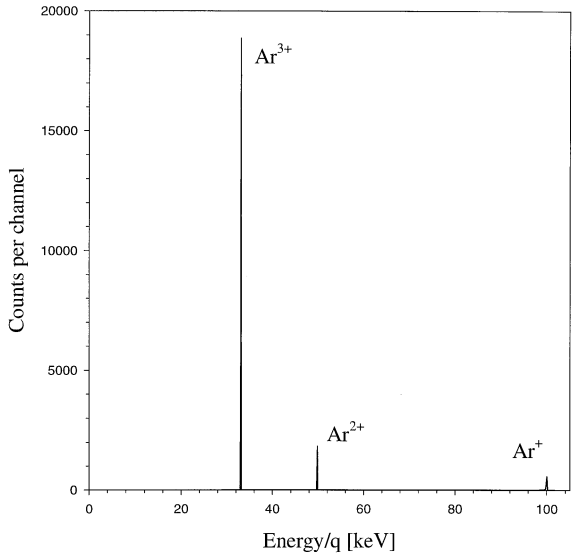

Fig. 2. Charge-state spectrum after 100 keV Ar^{3+}–C_{60} collisions at a target temperature of 430 °C. Not visible in this figure are the low-energy tails on the Ar^{+} and Ar^{2+} peaks.

curve as measured by Abrefah et al. [21]. Because the properties of solid C_{60} under heating are not fully understood, we have given special attention to this issue, and below our choice of the Abrefah relation among other possibilities is motivated by experimental findings. The primary beam was collimated by a rectangular slit situated upstream of the C_{60} target. After passing through the target the ionic charge-states in the beam could be monitored by means of a hemispherical electrostatic analyzer equipped with a channeltron detector. The acceptance angle of the analyzer was set at 0.4° by the preceding aperture. A second rectangular slit was mounted between the C_{60} cell and the electrostatic analyzer, making it possible to further confine the observed scattering angles. In the cross-section measurements the latter slit was always kept wide open. Distributions of the final ionic charge states were recorded by scanning the analyzer voltage step-wise and counting the number of detected ions at each step (fixed voltage) during a constant dwell time. A typical charge-state distribution following 100 keV Ar^{3+}–C_{60} collisions is displayed in Fig. 2, in which the Ar^{+} and Ar^{2+} peaks correspond to capture of 2 and 1 electrons, respectively. There is also information about the translational energies of the ions in the peak structures. The Ar^{2+} and Ar^{+} peaks in Fig. 2 are actually asymmetric (not visible in this figure) with tails extending to several kiloelectronvolts on their low-energy sides. To determine absolute cross sections we scanned over individual peaks at different target temperatures in the 380–480 °C interval. Background values at "zero" C_{60} pressure were obtained at 300 °C. Capture cross-sections $\sigma_{i,j}$ ($X^{i+} \rightarrow X^{j+}$, i.e. stabilized capture of i–j electrons from C_{60} by X^{i+}) were derived from the ratios $R(\mu)$ between the areas of the charge-reduced peaks and the primary peak, where the target thickness μ is calculated from the measured target temperature by the Abrefah relation [21]. To account for the relatively longer scan times over peaks of lower charges the peak areas were multiplied by a factor j/i (≤ 1). The actual cross-sections $\sigma_{i,j}$ were determined from the $\mu \rightarrow 0$ limit in a plot of

$$[R(\mu) - R(0)]/\mu$$

versus μ [23], where $R(0)$ is the background ratio obtained at 300 °C. Attenuation cross-sections σ_i, i.e. total cross sections for charge change of X^{i+}, were simply determined from the exponential decrease of the primary beam with increasing target thickness, $\sim\exp(-\mu\sigma_i)$. The measured capture and attenuation cross sections are listed in Table 1. The low-energy

Table 1
Measured capture and depletion cross-sections[a]

Cross section (10^{-15} cm^2)	Projectile		
	He	Ar	Xe
σ_1	23		
σ_2	22	31	
σ_3			44
$\sigma_{2,1}$	15	23	16
$\sigma_{3,2}$		26	25
$\sigma_{3,1}$		8	9
$\sigma_{4,3}$		30	25
$\sigma_{4,2}$		15	8
$\sigma_{4,1}$		10	8

[a] The uncertainty is estimated as 20% (not including possible errors of the used C_{60} vapor pressure curve [21]). The collision energy was 100 keV, except for the four-times charged projectile ions where it was 133 keV.

tails of peaks after electron capture were scanned in detail for various precursor ions at 100 keV and a temperature of 430 °C. Results from these measurements are presented in Sec. 3.3. In some cases the accepted scattering angles were confined by narrowing the rectangular exit slit symmetrically around the outgoing beam from the target.

3. Results and discussion

3.1. C_{60} vapour pressure in the target cell

It is essential for a correct determination of absolute cross sections to know the temperature dependence of the C_{60} density in the target. Several authors [21,24–26] have reported an irreversible change from one vapour pressure curve (first step) to another one (second step) when solid C_{60} is heated above a certain "transition" temperature. This temperature is about 477 °C according to Coheur et al. [26] but is given as an interval, 427–467 °C, in the report of Popovíc et al. [25]. Abrefah et al. [21] interpreted this as evaporation of remaining solvent and therefore identified the second curve as the true C_{60} vapour pressure relation. Their numerical results of the curve in the first step are not given in the paper. Later it was argued [24,25] that the amount of impurity in the C_{60} sample is too little to give such effects and that instead the very low trace of solvent somehow induces a permanent modification of the C_{60} powder, implying that the first curve is the correct one. This is supported by the fact that carefully purified (redistilled) C_{60} samples do not show the peculiar change of the temperature–pressure curve. Nevertheless, the task here is to correctly establish the present C_{60} target density from the measured temperature, which does not necessarily imply that the correct vapour pressure curve for absolutely pure solid C_{60} should be used. In previous collision experiments by us and others [5,20], the Abrefah relation has been used for this purpose. From a comparison between light absorption measurements and various C_{60} vapour pressure data in the literature Coheur et al. [26] found recently that the first Piacente curve [24] gives the best description of the temperature-pressure behaviour of pure C_{60}. Therefore, it is important to justify our choice of the Abrefah relation in the present study also.

We have in this and previous works [9,11] preheated the target to temperatures of about 500 °C for a couple of hours to get stable pressure conditions in the target. That is, according to the curve transition temperature of 477 °C we should use one of the vapour pressure curves reported for the second step, i.e., the second curve by Piacente et al. [24] or one of the curves by Abrefah et al. [21] or Mathews et al. [27]. The choice of curve will have a significant influence on the size of the determined cross sections because the maximum and minimum pressure values from the three curves differ by roughly a factor 2 in the present temperature interval 390–480 °C. We have no possibility of checking the absolute C_{60} pressure in the present experiment but the relative temperature dependence can be obtained from the yield of charge-changed ions under single collision conditions. In Fig. 3, the background-subtracted Ar^+ yield after 100 keV Ar^{2+}–C_{60} collision is compared with the C_{60} target thickness μ as calculated by available temperature-pressure relations given in the literature. The logarithms of the thickness and the yield have been plotted versus the inverse temperature with the same scaling of the y axes. The Ar^+ yield was obtained in two series: series A before preheating of the target and series B afterward. Primarily we focussed on the latter series because the cross-sections were determined under the same conditions. By comparing the slope of series B in Fig. 3 with the available vapour pressure curves for the second step (Mathews [27], Abrefah [21], or second Piacente curve [24]) we find the best agreement with the slope of the Abrefah curve, a strong indication that the pressure dependence on the temperature in our experiment is best described by that relation. Noteworthy here is that the Abrefah curve is based on data points in the 400–600 °C range, which (in contrast to the Piacente measurement range of 480–680 °C) covers almost the whole present temperature interval of 380–480 °C. By correcting the series B yields for double collisions (Fig. 3) we achieve perhaps an even better agreement with the Abrefah curve. The offsets of the two y axes

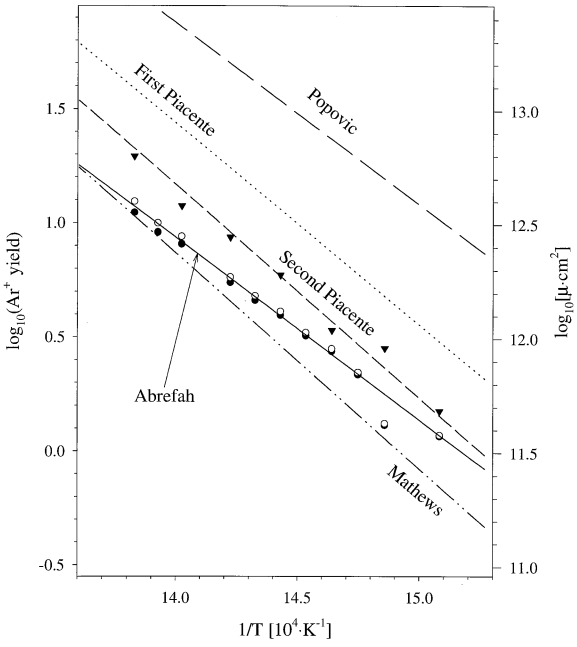

Fig. 3. Comparison of the measured Ar^+ yield in 100 keV Ar^{2+}–C_{60} collisions and the target thickness μ as calculated using C_{60} vapour pressure curves available in the literature [21,24,25,27]. The $I_+(I_+ + I_{2+})$ ratio is taken as the Ar^+ yield, where I_+ and I_{2+} are the respective beam intensities of Ar^+ and Ar^{2+}. A measure of the background yield from rest-gas collisions was recorded at 300 °C and has been subtracted from the other data points. The logarithmic values of both the yield (left axis) and the target thickness (right axis) are plotted vs. the inverse target temperature $1/T$. The measured points in series A (before heating to 480 °C) and B (after heating to 480 °C) are displayed as filled triangles and circles respectively. The relations between μ and $1/T$ obtained from the different vapour pressure curves are shown with lines as follows: Mathews et al. [27], dash-dot-dot; Abrefah et al. [21], solid; second curve in Piacente et al. [24], dashed; first curve in Piacente et al. [24], dotted; Popovíc et al. [25], long dashes. Of these curves, the three mentioned first relate to a second thermal step, i.e. after the irreversible change of the C_{60} vapour pressure curve has occurred. Double-collision corrected yields in series B are displayed as open circles. The corrected yields were obtained by dividing the uncorrected yields by a correction factor $c = [1 - (\sigma_2 + \sigma_1)\mu]$, see e.g. Heinemeier et al. [23], where the curve of Abrefah et al. [21] was used to calculate μ, and $\sigma_2 + \sigma_1$ was approximated by $\sim 25 \times 10^{-15}$ cm^2 (Table 1). The correction factors are about 0.99, 0.95, and 0.90 at temperatures 400 °C, 430 °C, and 450 °C, respectively. The scaling of the two y axes is the same but their off-sets have been adjusted to match the corrected series B points (open circles) with the Abrefah curve [21].

in Fig. 3 have been adjusted to overlap the corrected series B data with the Abrefah curve. Finally, we remark that measuring the target density variation with temperature by the present ion-beam technique actually can be used as an alternative method to determine heats of sublimation [21]. Because of the good agreement between the series B data and the Abrefah curve [21] we find here that the C_{60} heat of sublimation after preheating is close to the value reported by Abrefah et al. [21], 38 ± 1 kcal/mol.

3.2. Electron capture

The collision velocities in this study are in the range 0.1–0.4 a.u., which is lower than typical velocities of the outermost electrons in C_{60}. In this slow-collision regime, the total reaction cross section in collisions of multiply charged ions on *atomic* targets is dominated by electron capture. The capture radii go far outside the extension of the ionic electron cloud and are set by the range of the Columb potential and the binding energies of the outer target electrons. The gross features of the capture process in ion–atom collisions can be quantified in the atomic over-the-barrier model [28,29], where it is assumed that the first electron is transferred from the target atom to the ion at a distance where its binding energy becomes lower than the potential barrier between the particles. The total capture cross section in the over-the-barrier model for atoms is given as

$$\sigma = \pi {R_1}^2 = \pi[(1 + 2\sqrt{q})/I_1]^2 \quad (1)$$

in atomic units, where R_1 is the capture radius, I_1 the first ionization energy, and q the ionic charge. We now discuss whether a similar, or perhaps even exactly the same, picture may be applied to ion–C_{60} collisions.

Using the C_{60} ionization energy of 7.6 eV in Eq. (1) we obtain total cross-sections of 10×10^{-15}, 16×10^{-15}, 22×10^{-15}, and 28×10^{-15} cm^2 for $q = 1$, 2, 3, and 4, respectively. Comparing these values with our experimental attenuation cross-sections σ_1, σ_2, and σ_3 in Table 1, it appears that the over-the-barrier model for atoms underestimates the cross-sections. The total cross-sections for four-times charged projectile ions were not measured, but lower limits of σ_4 can be estimated as 55×10^{-15} cm^2 for Ar and $41 \times$

10^{-15} cm^2 for Xe by summing the individual capture cross-sections $\sigma_{4,3}$, $\sigma_{4,2}$, and $\sigma_{4,1}$. These summed cross sections are also significantly larger than the estimate from the classical over-the-barrier model. Thus, it seems that the atomic over-the-barrier model somehow must be modified to account for the larger total cross sections observed in the experiment. Let us therefore recapitulate how electron capture has been dealt with in previous works on similar collision systems.

Walch et al. [20] collided slow (80-keV) ions of higher charge, Ar^{8+}, with C_{60} in a pioneering study of electron capture from fullerene molecules. They obtained a total cross-section $(44 \pm 18) \times 10^{-15}$ cm^2 that permitted them to normalize the signals from extracted recoil C_{60}^{q+} ions and thereby derive individual capture cross sections. The data were analyzed in the over-the-barrier picture by treating C_{60} both as an atom and as a metal sphere. No strong preference for either case was observed and it was therefore concluded that the normal atomic model [28,29] gives a fairly good description of the capture processes. Recently, total cross sections and energy-gain distributions for $(3.3 \times q)$ keV Ar^{q+}–C_{60} (q = 8, 13–15) collisions were reported by Selberg et al. [11], who considered also the discrete nature of the electronic capture states in a potential-curve analysis. Their measured total cross-section $(46 \pm 14) \times 10^{-15}$ cm^2 for Ar^{8+} on C_{60} is in good agreement with the value given by Walch et al. [20]. By using the energy-gain information about the final quantum states and curve-crossing arguments Selberg et al. [11] investigated the charge localization within the created positive C_{60} ions at various stages during the collision. The main conclusion was that the positive hole left on the C_{60} surface (closest to the Ar ion) by the first transferred electron remains fixed in position during the actual transfer, a result that is independent of the hole mobility subsequent to the electron transfer. The contradictory agreement with the atomic over-the-barrier model in the study by Walch et al. [20] for the same value of the Ar^{8+} cross section as in the work by Selberg et al. [11] is most probably caused by neglect of the discrete nature of the final capture states by Walch et al. [20].

The ideas presented by Selberg et al. [11] were to a large extent based on conclusions drawn in an earlier experiment by Shen et al. [9]. Shen et al. [9] studied single- and double-electron capture in collisions of multiply charged C_{60} and C_{70} ions on atomic and C_{60} targets. The measured cross sections agreed well with a model in which the fullerene charges are localized and mobile on the collision time scale. That is, the charges move freely about on the molecular surface to minimize the electrostatic energy, but (as found also by Selberg et al. [11]) during the much faster transfer events the charges are frozen. The picture given by Shen et al. [9] of mobile and localized fullerene charges has later been confirmed by Cameron and Parks [12], who studied electron capture from atomic beams by trapped C_{60} ions and found that the capture cross section was independent of the C_{60} charge (from +1 to +3). To summarize, the results of Shen et al. [9], Selberg et al. [11], and Cameron et al. [12] point toward a common picture of the mobility of the fullerene charges. The relaxation time of the charges is faster than the collision time ($\sim 10^{-14}$ s) but slower than the electron transfer time, which is believed to be 10^{-16}–10^{-17} s and determined by the Bohr velocity and the distance from C_{60} to the top of the potential barrier between the colliding particles.

Returning now to the present data we would like to see whether the concept from Selberg et al. [11] of a static hole during the transfer of the first electron applies also in our case with lower charged ions. For simplicity we will not invoke the curve-crossing picture of Selberg et al. [11] but stick to the over-the-barrier model, with the assumption of a quasicontinuum of capture states on the projectile ion. In the following we will attempt to incorporate the picture of a singly charged positive hole localized on the surface of the C_{60} molecule during the transfer of the first electron to the atomic ion (Eq. (1)):

$$\sigma = \pi R_1^2 = \pi[(1 + 2\sqrt{q})/I_1 + R_0]^2 \qquad (2)$$

where R_0 is the C_{60} cage radius (6.7 a.u.). Note that the capture radius is simply extended by the cage radius compared with the original model and that the

sensitivity of the total cross section on R_0 becomes larger with decreasing q. The latter was one of the main motivations behind the present experiment. Calculating total cross sections with Eq. (2) gives 27×10^{-15}, 37×10^{-15}, 45×10^{-15}, and 53×10^{-15} cm^2 for $q = 1$, 2, 3, and 4, respectively. The agreement with the measured cross sections (Table 1) now becomes better, which lends some support to the conclusions of Selberg et al. [11] and Shen et al. [9]. However, we stress here that this conclusion relies heavily on the choice of vapour pressure curve for C_{60}. This was discussed in detail in Sec. 3.1 where we argue that the Abrefah curve [21] was the best choice in the present case but also point out that there is no independent information on the absolute value of the vapour pressure.

It was shown by Selberg et al. [11] that the size of the total cross section is far more sensitive to the mobility of the created positive hole than to the induced polarization of the C_{60} electron cloud. This justifies the omission of polarization effects in Eq. (2) for the high ionic charges that were treated by Selberg et al. [11]. To be sure that the effects of the polarization also can be neglected for collisions with lower charged ions we have estimated the potential-barrier height for the first transferred electron in Xe^{3+}–C_{60} collisions under different conditions. (1) According to the modified over-the-barrier model (as well as the measured σ_3 value) the capture radius R_1 is 23 a.u. and the distance between the target and the top of the barrier 13 a.u. The potential experienced at the top of the barrier by the first transferred electron is then -12.5 eV. This value is obtained by adding the potentials from the Xe^{3+} projectile and the C_{60}^+ target under the assumption that the charge on C_{60}^+ is situated on the cage surface closest to the projectile. We now compare the results from this model with (2) the original atomic over-the-barrier model where the charge is in the C_{60}^+ centre and (3) the same model as in (2) but where the induced polarization of the C_{60}^+ electron cloud is taken into account. The exact electron potential in the latter case is not known and therefore a maximum estimate of the polarization effect is obtained by treating C_{60} as a metal sphere [10]. In Fig. 4 the electron potentials in the three

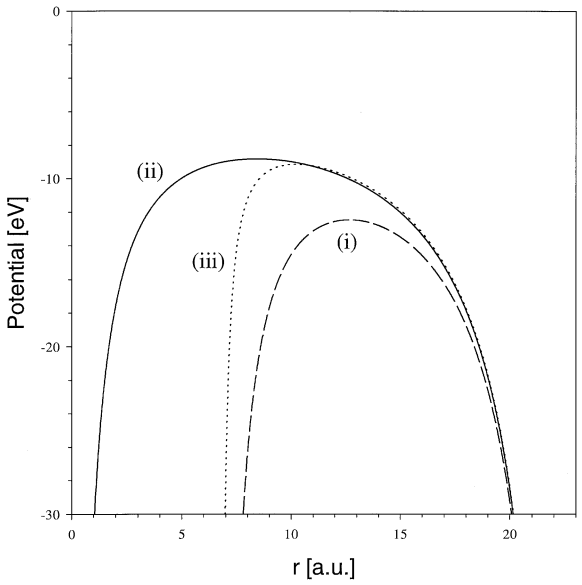

Fig. 4. Potential energy of the first transferred electron from C_{60} to Xe^{3+} versus r, the distance from the electron to the center of C_{60}^+, at an intermolecular separation 23 a.u. The potential curves are calculated in three ways (see text): (i) the C_{60}^+ charge localized on the surface closest to the Xe ion, no electron polarization (dashed line); (ii) the C_{60}^+ charge localized in the centre of the molecule, no electron polarization (solid line); and (iii) C_{60}^+ treated as a metal sphere (dotted line).

different situations are plotted as a function of the electron position r (i.e. the distance from the C_{60}^+ centre to the electron on the Xe^{3+}–C_{60}^+ axis) for an intermolecular separation of 23 a.u., which is equal to R_1 in Eq. (2). The (1) and (3) potentials diverge at the cage surface ($r = 6.7$ a.u.) but the polarization forces are short-range and at the barrier top of the (1) potential ($r = 10$ a.u.) there is no longer any visible difference between the potentials of the normal model (2) and the polarization model (3). The important conclusion is that the localization of the C_{60}^+ charge during the electron transfer has a much greater influence on the barrier height than does the induced polarization of the electron cloud (see the three barriers in Fig. 4). This picture also remains valid when other projectile charges and intermolecular separations are considered.

A quantified analysis of multiple capture is difficult for several reasons. Autoionization of multiply

excited states before the detector will tend to underestimate capture of many electrons. In addition it is not obvious how to treat the positive charges of C_{60} after the first electron has been transferred. We note that the relative contribution from stabilized multiple capture to the total cross-section is larger with C_{60} as target than with ordinary mono- and diatomic targets. This can be corroborated by comparing the relative intensities of different charge states after collisions with C_{60} and rest-gas molecules (cold target cell). The ions that penetrate a single C_{60} molecule experience an average target thickness of 15×10^{15} C atoms per cm^2 (see next section), which at our collision velocities is sufficient to obtain a so-called equilibrium charge-state distribution. For 100 keV Ar exiting a carbon foil the equilibrium charge-state distribution is characterized by roughly 40% neutral Ar, 45% Ar^+, and 15% Ar^{2+} [30]. In other words, the contribution to the Ar^+ production from cage-penetrating collisions should be about 2×10^{-15} cm^2 (the geometrical cage cross section is 4×10^{-15} cm^2), irrespective of the charge of the primary ion. The corresponding number for the Ar^{2+} production is 0.6×10^{-15} cm^2. The measured $\sigma_{4,1}$ and $\sigma_{3,1}$ cross sections (Table 1) are about 9×10^{-15} cm^2, so corepenetrating collisions are seen to contribute appreciably to these cross sections. We return to this point in the following section. It should also be stressed that multiple capture is likely to be enhanced in distant collisions with C_{60} as compared with mono- and diatomic targets. This is caused by the small differences (about 4 eV [15]) between succeeding ionization potentials of C_{60}. That is, C_{60} acts as a rich source of loosely bound electrons.

3.3. Energy loss

The overwhelming fraction of the capture events take place in collisions where the impact parameter is larger than the C_{60} radius, as can be understood from a comparison of the total cross-sections in Table 1 with the geometrical cage cross-section 4×10^{-15} cm^2 (the cross-section of the nuclear framework). In these nonviolent collisions the projectile ions gain translational energies of 1–100 eV through Coulumb repulsion between the two positively charged particles [11]. This is too little to be observed in our experiment because we have a minimum energy width of about 200 eV for the primary peak. However, the electron-capture peaks have tails on the low-energy sides that range to several kiloelectronvolts (Fig. 5). These tails are particularly prominent for the peaks of ions that are singly charged after electron capture. Other mechanisms than the above must be invoked to explain the negative sign and the large size of the energy change, and quite naturally one associates the tails with close collisions where the ion penetrates the cage or passes in its immediate vicinity. Thus, there are in principle two possibilities: elastic binary encounters between the precursor ion and individual C atoms in C_{60} and inelastic electronic processes, i.e. ionization and excitation. We have previously discussed the competition between these energy-loss mechanisms in conjunction with fragmentation after 50 keV collisions between C_{60} ions and noble gas atoms [7]. The collision velocity in that work, $0.05v_0$, was lower than in this work and it was concluded from the theory of particle stopping in matter that the elastic contribution is predominant. At the present

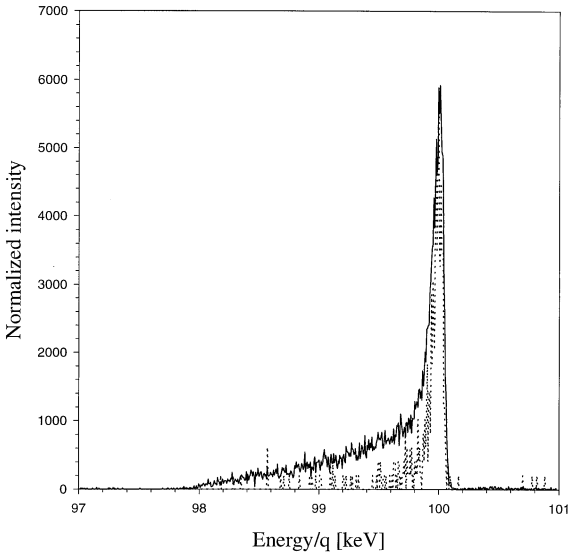

Fig. 5. Detailed scan over the 100 keV $Ar^{3+} \rightarrow Ar^+$ peak with (solid line) and without (dotted line) C_{60} in the target cell. The peak heights have been normalized.

velocities ($0.32v_0$ for 100 keV Ar) the situation is different because the cross-sections for inelastic processes depend linearly on the collision velocity at the same time as the velocity for maximum elastic energy loss is passed. Therefore, the relative importance of inelastic processes is increased, although the elastic part of the stopping cross section is still larger by a factor of 3. Following the treatment of Larsen et al. [7], using an r^{-2} potential in the Lindhard model for elastic stopping, we calculate the transferred energy in 100 keV Ar–C encounters as 71 keV, 4.2 keV, and 12 eV for impact parameters 0.0, 0.1, and 0.5 Å, respectively. Similarly we obtain inelastic energy loss of 169, 111, and 28 eV for the corresponding impact parameters by the Firsov formula [31]. The rather weak inelastic impact parameter dependence suggests that the inelastic energy loss for a cage-penetrating 100 keV Ar ion is almost independent of its trajectory. The elastic energy loss is, however, extremely sensitive to the ion trajectory through the cage because there is a strong impact parameter dependence of the transferred elastic energy in a binary Ar–C encounter. Therefore, a very broad elastic energy-loss distribution is expected for cage-penetrating ions and often (as in this work) it is more relevant to use the *most probable* elastic energy loss instead of the *average* value, which is heavily weighted by rare high energy-loss events (see Fastrup et al. [22] and references therein). It will become clear that these rare events are associated with scattering angles so large that they cannot be detected in many experimental situations, e.g. the present one.

Fastrup et al. [22] determined the inelastic stopping cross section for 138-keV Ar in graphite as 53.4×10^{-15} eV cm^2/atom by the beam-foil technique. Let us assume that the projected C atom density in C_{60} is homogenous over the cage cross section, giving a target thickness of $(60/4) \times 10^{15}$ cm^{-2} for a single C_{60} molecule. Using this value and the cross section by Fastrup et al., we arrive at an average inelastic loss of 800 eV for a cage-penetrating 138 keV Ar ion. This estimate of the inelastic loss is uncertain for several reasons. For instance, the collision velocity is somewhat higher than in the present systems and the real projected C atom density is higher at the cage edges than in the centre. Despite this we believe that 800 eV is a rather good estimate of the order of size for the inelastic energy loss of a cage-penetrating 100 keV Ar ion. The calculated most probable elastic contribution to the stopping cross section for 138 keV Ar in graphite is given as 10.1×10^{-15} eV cm^2/atom by Fastrup et al. [22]. Note that this value is only 20% of the inelastic stopping cross section whereas the average elastic stopping cross section is a factor of 3 larger than the inelastic one. This means that the inelastic contribution to the energy loss will dominate for *most* of the cage-penetrating ions, although a few will experience close binary encounters and elastically lose more than 10 keV in translational energy.

No tails in the present experiment are generated in collisions on rest-gas molecules, as illustrated in Fig. 5 by the shape of the 100 keV $Ar^{3+} \rightarrow Ar^{+}$ peak recorded with and without C_{60} in the target. Neither have we seen any signs of such tails in previous experiments of this kind with atomic and diatomic target particles. It thus seems that the tails are signatures of the C_{60} target. We have studied in particular the tails on the Ar^{+} and Ar^{2+} peaks after 100 keV Ar^{3+}–C_{60} collisions (Fig. 6). In Fig. 6(a) the peaks have been normalized to each other, and it is clear that the relative contribution from the tail is much greater for Ar^{+} than for Ar^{2+}. It is a general observation also with other precursors than Ar^{3+} that the tails are most pronounced on the peaks of singly charged ions. This is in line with the tails being due to cage collisions because the capture radius shrinks with the number of captured electrons. The Ar^{+} and Ar^{2+} peaks are shown with the same intensity scale in Fig. 6(b), from which it is evident that processes leading to large energy loss more often result in Ar^{+} than in Ar^{2+}. The $Ar^{3+} \rightarrow Ar^{+}$ cross-section $\sigma_{3,1}$ (Table 1) is larger than the geometrical cross-section and therefore the double-capture radius should also be larger than the cage radius. Accordingly, we would not expect large energy loss in the distant single-capture events. It could be that the Ar^{2+} tail is due to autoionizing double capture but unfortunately we cannot discriminate between this process and pure single capture in the present experiment. Alternatively, the Ar^{2+} tail can be explained by treating C_{60} as a microscopic foil.

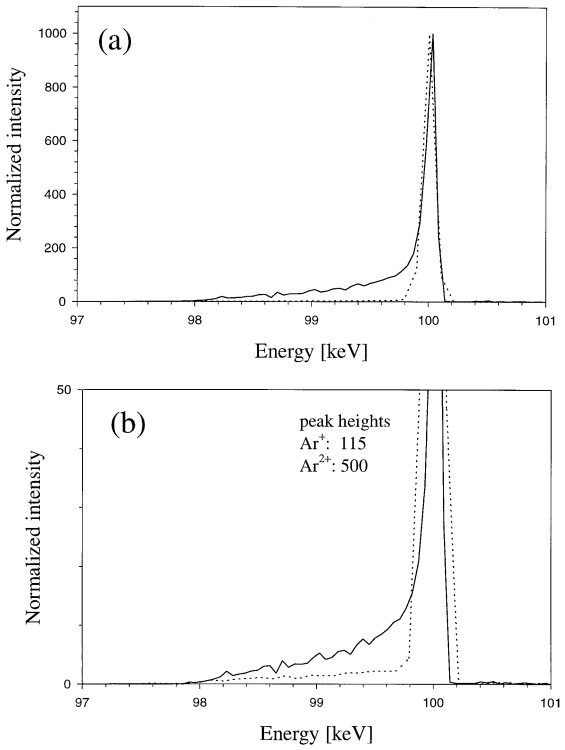

Fig. 6. Detailed scans over the 100 keV $Ar^{3+} \rightarrow Ar^{+}$ peak (solid lines) and $Ar^{3+} \rightarrow Ar^{2+}$ peak (dotted lines) with C_{60} in the target cell. (a) The peak heights have been normalized; (b) the peaks have the correct relative intensities.

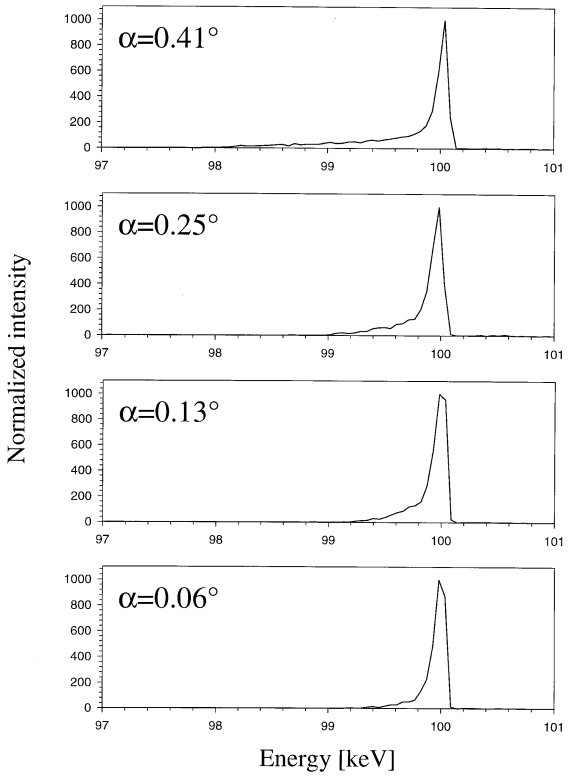

Fig. 7. Detailed scans over the 100 keV $Ar^{3+} \rightarrow Ar^{+}$ peak as a function of the acceptance angle α of the electrostatic analyzer. The scattering angles were confined by narrowing the adjustable rectangular exit slit (Fig. 1) symmetrically around the outgoing beam from the target. The α values in the figure relate to ion trajectories through the corners of the quadratic hole of the exit slit, i.e. the maximum possible scattering angles. The peak heights have been normalized.

If we assume that cage-penetrating ions always reach charge-state equilibrium (see Sec. 3.2), then the tail shapes for Ar^{+} and Ar^{2+} are expected to be similar but the intensity in the Ar^{2+} tail should be only 33% of the one for Ar^{+}, according to the measured equilibrium charge-state distributions given by Turkenburg et al. in [30] (see the relative Ar^{+} and Ar^{2+} abundances given in the previous section). These predictions are seen to be in good accord with experimental observations [Fig. 6(b)], which suggests that there are no differences between ion trajectories that lead to the Ar^{+} and Ar^{2+} tails.

One way of getting information about the nature of the energy-loss mechanism is to investigate the relation between lost energy and projectile scattering angle (see e.g. Johnson [32]). The tails can gradually be cut away by reducing the angular acceptance, which shows that as a general trend the energy loss increases with scattering angle at the same time as the ionic intensity decreases (Fig. 7). The maximum accepted scattering angle in the setup is 0.4 °. If we assume first that the tail events stem from only one elastic Ar–C encounter in a C_{60} molecule, then the maximum transferred energy that can be detected is as small as 20 eV, and to account for the observed energy loss of up to 2 keV would require a 4 ° acceptance. Therefore, it seems impossible that pure single elastic encounters can account for the tails, which may instead be multiple encounters (in one C_{60} molecule) with a net scattering in the forward direction. However, it is clear that many *purely* elastic

events with several hundred eV energy losses would have too large scattering angles to be detected. From a comparison of the tail areas and the total peak areas in Fig. 5 with the measured $\sigma_{3,2}$ and $\sigma_{3,1}$ cross sections (Table 1) we find that the total tail cross-section is approximately equal to the geometrical cross section of C_{60}. This indicates that most of the cage-penetrating collisions are observed and, consequently, that the energy loss in these collisions cannot be accounted for by elastic energy transfer only. The kinematics in the inelastic processes is different. Large amounts of energy can be transferred inelastically to C_{60} without severe ion scattering, provided that the simultaneous elastic contribution is small. The beam-foil results discussed above indicate that the inelastic part is predominant for most of the cage-penetrating ions. In addition, the size of the predicted inelastic loss, ~800 eV, agrees well with what is measured here. It thus appears that inelastic electron processes give the predominant contribution to the observed energy loss in collisions between 100 keV Ar^{3+} and C_{60}. The Ar^{+} tail (not shown in figure) after 100 keV Ar^{2+}–C_{60} collisions has both the same shape and cutoff as the tails generated with 100 keV Ar^{3+}, showing that the charge of the precursor ion is irrelevant for the stopping process.

Finally, the 100 keV $CO_2^{2+} \rightarrow CO_2^{+}$ peak was scanned with and without C_{60} in the target cell (Fig. 8). A tail is also observed here which raises the question of how a molecule can survive a cage impact where it loses as much as 1 keV of translational energy. It is reasonable that the three atoms are slowed down equally and scattered in the same direction. Such a coherent behaviour is hard to imagine with the impact-parameter sensitive elastic processes and therefore the mere existence of a tail on the $CO_2^{2+} \rightarrow CO_2^{+}$ peak is strong evidence of the inelastic predominance in the ionic stopping.

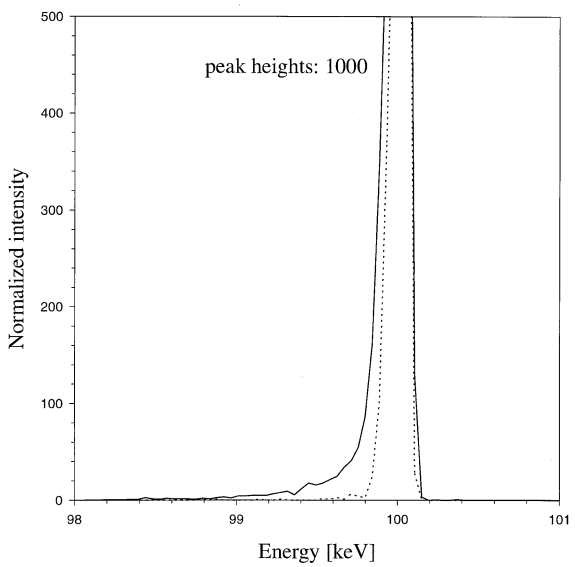

Fig. 8. Detailed scan over the 100 keV $CO_2^{2+} \rightarrow CO_2^{+}$ peak with (solid line) and without (dotted line) C_{60} in the target cell. The peak heights have been normalized.

4. Conclusions

Electron capture and accompanying energy loss have been investigated for 100 keV ion–C_{60} collisions with ionic charges from +1 to +4. To determine absolute attenuation and capture cross-sections we have used the Abrefah vapour pressure curve for C_{60} [21]. This choice was partly motivated by the good agreement (on a relative scale) between this curve and the measured temperature dependence of the C_{60} density in the target vapour. Moreover, the Abrefah curve and our experimental data are both obtained after preheating of the C_{60} powder. Relying on the Abrefah curve we arrive at experimental cross-sections that are significantly larger than those predicted by the atomic over-the-barrier model [28,29]. This discrepancy can be accounted for by applying the concept from Shen et al. [9] and Selberg et al. [11] of static localized charges on the C_{60} molecule *during* the transfer of an electron. This result must, however, be regarded as provisional until the issue of the C_{60} vapour pressure is resolved. Note that the results summarized below about ionic energy loss are independent of the absolute calibration of the cross-section scale.

Large numbers of the ions that capture electrons lose several hundred electronvolts in translational energy. This energy loss is attributed mainly to inelastic electron excitation and ionization. We are

able to distinguish between these processes and elastic binary encounters from intensities and scattering angles of the slowed-down ions. Further support for the predominance of the inelastic contribution to the energy loss comes from a comparison with beam-foil data and theoretical estimates and that molecular ions can survive cage-penetrating collisions. To learn more about the detailed energy-loss mechanisms it would be appropriate to undertake careful studies of the energy-scattering angle relation in a much broader scattering angle regime than covered here.

Acknowledgements

This work was supported by the Danish National Research Foundation through the Aarhus Center for Advanced Physics (ACAP) and the Swedish Natural Science Research Council (NFR).

References

[1] R.J. Doyle Jr., M.M. Ross, J. Phys. Chem. 95 (1991) 4954.
[2] P. Hvelplund, L.H. Andersen, H.K. Haugen, J. Lindhard, D.C. Lorents, R. Malhotra, R. Ruoff, Phys. Rev. Lett. 69 (1992) 1915.
[3] T. LeBrun, H.G. Berry, S. Cheng, R.W. Dunford, H. Esbensen, D.S. Gemmell, E.P. Kanter, Phys. Rev. Lett. 72 (1994) 3965.
[4] R. Ehlich, M. Westerburg, E.E.B. Campbell, J. Chem. Phys. 104 (1996) 1900.
[5] F. Rohmund, A.V. Glotov, K. Hansen, E.E.B. Campbell, J. Phys. B 29 (1996) 5143.
[6] R. Ehlich, O. Knospe, R. Schmidt, J. Phys. B, to be published.
[7] M.C. Larsen, P. Hvelplund, M.O. Larsson, H. Shen, unpublished.
[8] S. Petrie, J. Wang, D.K. Bohme, Chem. Phys. Lett. 204 (1993) 473.
[9] H. Shen, P. Hvelplund, D. Mathur, A. Bárány, H. Cederquist, N. Selberg, D.C. Lorents, Phys. Rev. A 52 (1995) 3847.
[10] A. Bárány, C.J. Setterlind, Nucl. Instrum. Methods Phys. Res. B 98 (1995) 184.
[11] N. Selberg, A. Bárány, C. Biedermann, C.J. Setterlind, H. Cederquist, A. Langereis, M.O. Larsson, A. Wännström, P. Hvelplund, Phys. Rev. A 53 (1996) 874.
[12] D.B. Cameron, J.H. Parks, Chem. Phys. Lett. 272 (1997) 18.
[13] U. Thumm, A. Bárány, H. Cederquist, L. Hägg, C.-J. Setterlind, Phys. Rev. A 56 (1997) 4799.
[14] F. Rohmund, E.E.B. Campbell, J. Phys. B 30 (1997) 5293, and references therein.
[15] P. Scheier, B. Dünser, T.D. Märk, Phys. Rev. Lett. 74 (1995) 3368.
[16] R.K. Janev, H. Winter, Phys. Rep. 117 (1985) 265.
[17] J. Burgdörfer, in C.D. Lin (Ed.), Review of Fundamental Processes and Applications of Atoms and Ions, World Scientific, Singapore (1993).
[18] L. Hägg, C.O. Reinhold, J. Burgdörfer, Phys. Rev. A 55 (1997) 2097.
[19] J.-P. Briand, S. Thuriez, G. Giardino, G. Borsoni, V. Le Roux, M. Froment, M. Eddrief, C. de Villeneuve, B. D'Etat-Ban, C. Sébenne, Phys. Rev. A 55 (1997) R2523.
[20] B. Walch, C.L. Cocke, R. Voelpel, E. Salzborn, Phys. Rev. Lett. 72 (1994) 1439.
[21] J. Abrefah, D.R. Olander, M. Balooch, W.J. Siekhaus, Appl. Phys. Lett. 60 (1992) 1313.
[22] B. Fastrup, P. Hvelplund, C.A. Sautter, Mat. Fys. Medd. Dan. Vid. Selsk. 35 no. 10 (1966).
[23] J. Heinemeier, P. Hvelplund, F.R. Simpson, J. Phys. B 9 (1976) 2669.
[24] V. Piacente, G. Gigli, P. Scardala, A. Giustini, D. Ferro, J. Phys. Chem. 99 (1995) 14052.
[25] A. Popovíc, G. Drazic, J. Marsel, Rapid Comm. Mass. Spectrom. 8 (1994) 985.
[26] P.F. Coheur, M. Carleer, R. Colin, J. Phys. B 29 (1996) 4987.
[27] C.K. Mathews, M. Sai Baba, T.S. Lakshmi Narasimhan, R. Balasubramanian, N. Sivaraman, T.G. Srinivasan, P.R. Vasudeva Rao, J. Phys. Chem. 96 (1992) 3566.
[28] A. Bárány, G. Astner, H. Cederquist, H. Danared, S. Huldt, P. Hvelplund, A. Johnson, H. Knudsen, L. Liljeby, K.-G. Rensfelt, Nucl. Instr. Meth. B 9 (1985) 397.
[29] A. Niehaus, J. Phys. B 19 (1986) 2925.
[30] W.C. Turkenburg, B.G. Colenbrander, H.H. Kersten, F.W. Saris, Surf. Sci. 47 (1975) 272.
[31] E.S. Parilis, Nucl. Instr. Meth. Phys. Res. B 88 (1994) 21.
[32] R.E. Johnson, Introduction to Atomic and Molecular Collisions, Plenum, New York (1982).